

A single algorithm to retrieve turbidity from remotely-sensed data in all coastal and estuarine waters

A.I. I Dogliotti, K.G. G Ruddick, B. Nechad, D. Doxaran, E. Knaeps

▶ **To cite this version:**

A.I. I Dogliotti, K.G. G Ruddick, B. Nechad, D. Doxaran, E. Knaeps. A single algorithm to retrieve turbidity from remotely-sensed data in all coastal and estuarine waters. Remote Sensing of Environment, 2015, 156, pp.157-168. 10.1016/j.rse.2014.09.020 . insu-03190140

HAL Id: insu-03190140

https://insu.hal.science/insu-03190140

Submitted on 6 Apr 2021

HAL is a multi-disciplinary open access archive for the deposit and dissemination of scientific research documents, whether they are published or not. The documents may come from teaching and research institutions in France or abroad, or from public or private research centers.

L'archive ouverte pluridisciplinaire **HAL**, est destinée au dépôt et à la diffusion de documents scientifiques de niveau recherche, publiés ou non, émanant des établissements d'enseignement et de recherche français ou étrangers, des laboratoires publics ou privés.



Distributed under a Creative Commons Attribution - NoDerivatives 4.0 International License

Remote Sensing of Environment 156 (2015) 157–168

Contents lists available at ScienceDirect

Remote Sensing of Environment

journal homepage: www.elsevier.com/locate/rse

A single algorithm to retrieve turbidity from remotely-sensed data in all coastal and estuarine waters

A.I. Dogliotti [a,*], K.G. Ruddick [b], B. Nechad [b], D. Doxaran [c], E. Knaeps [d]

[a] Instituto de Astronomía y Física del Espacio (IAFE), CONICET/UBA, Argentina
[b] Royal Belgian Institute for Natural Sciences (RBINS), Operational Directorate Natural Environment, Belgium
[c] Laboratoire d'Océanographie de Villefranche (LOV), UMR 7093, CNRS/UPMC, France
[d] Flemish Institute for Technological Research (VITO), Belgium

ARTICLE INFO

Article history:
Received 4 April 2014
Received in revised form 9 September 2014
Accepted 13 September 2014
Available online 14 October 2014

Keywords:
Turbidity (*T*)
Water reflectance
Radiative transfer simulations
Uncertainty analysis
T algorithm validation
Southern North Sea
Scheldt
Gironde
Río de la Plata
French Guyana

ABSTRACT

Ocean color remote sensing has been shown to be a useful tool to map turbidity (*T*) and suspended particulate matter (*SPM*) concentration in turbid coastal waters. Different algorithms to retrieve *T* and/or *SPM* from water reflectance already exist, however there are important questions as to whether these algorithms need to be calibrated specifically for different regions. In the present work the potential generality of a semi-empirical single band turbidity retrieval algorithm using the near infrared (NIR) band at 859 nm in highly turbid waters is assessed. For completeness the use of 645 nm in medium to low turbidity waters is also proposed. Radiative transfer simulations and *in situ* measurements from various European and South American coastal and shallow estuarine environments characterized by high concentrations of suspended sediments are analyzed. Reflectance and turbidity measurements were performed in the southern North Sea (SNS) and French Guyana (FG) coastal waters, and Scheldt (SC), Gironde (GIR) and Río de la Plata (RdP) estuaries. Simulations showed that uncertainty for turbidity estimation associated with different particle types and bidirectional effects is typically less than 6%. When applied to field data from the five different sites, the semi-analytical algorithm performed well: turbidity estimates were within 12% and 22% of *in situ* values. A good performance was also found when the entire database was analyzed ($n = 106$) with a mean relative error of 13.7% and bias of 4.8%. The good performance of the algorithm for all these regions, despite differences in sediment characteristics, and the results of the radiative transfer simulations suggest the global applicability of the algorithm to map turbidity up to 1000 FNU. Consequently regional algorithms to retrieve *SPM* concentration from reflectance can be designed by combining this global algorithm to retrieve *T* from water reflectance with a regional relationship to convert *T* to *SPM*. This has the very practical advantage that the measurements needed to calibrate the latter *T*/*SPM* conversion for any new region are much easier and cheaper than *in situ* reflectance measurements.

© 2014 The Authors. Published by Elsevier Inc. This is an open access article under the CC BY-NC-ND license (http://creativecommons.org/licenses/by-nc-nd/3.0/).

1. Introduction

1.1. Motivation

There is a strong user interest in monitoring the turbidity of coastal and estuarine waters. Satellite mapping of turbidity is relevant both as an indicator of the optical environment for water quality monitoring purposes (Nechad, Ruddick, & Neukermans, 2009) and as an easily-measurable proxy for suspended particulate matter (*SPM*) concentration in sediment transport applications (Gippel, 1995). As regards water quality monitoring, turbidity is specifically listed as a mandatory parameter to be measured by EU member states in the Marine Strategy Framework Directive (European Union, 2008). Whereas various turbidity retrieval algorithms have been proposed for specific geographical regions as described in Section 1.2, the advent of large scale automated global processing of satellite data motivates the need for a single standard algorithm, valid everywhere, preferably without the need for region-specific adaptation or calibration. The objective of the present study is to determine whether a single algorithm for retrieval of turbidity can be valid for all coastal and estuarine waters, regardless of geographical region, particle type, size, composition, concentration, *etc.*

In the present study the term "turbidity" follows the definition of the International Standards Organization ISO 7027 (ISO, 1999), using the 90° side-scattering of light at 860 nm with respect to Formazin, a chemical standard. It is important to note the advantages of this definition as opposed to alternative definitions. For example, the definition of EPA (1993) is based on broadband scattering of light from a tungsten lamp and is thus much more sensitive to particle composition. It is also noted that the ISO definition gives an inherent optical property, in

* Corresponding author.
E-mail address: adogliotti@iafe.uba.ar (A.I. Dogliotti).

http://dx.doi.org/10.1016/j.rse.2014.09.020
0034-4257/© 2014 The Authors. Published by Elsevier Inc. This is an open access article under the CC BY-NC-ND license (http://creativecommons.org/licenses/by-nc-nd/3.0/).

contrast to related apparent optical properties such as diffuse attenuation or Secchi depth, which are sensitive to the ambient light field (sun zenith angle, *etc.*). A drawback of the ISO definition is the use of a chemical reference, giving Formazin Nephelometric Unit (FNU), rather than a physical reference, giving units of m^{-1}. While a simple and unique conversion factor between FNU and m^{-1} could be defined from measurement of the 90° scattering coefficient of Formazin in m^{-1}, such a measurement has not yet been made at 860 nm to our knowledge.

1.2. Algorithms for retrieval of turbidity

Many remote sensing studies have been devoted to retrieve *SPM*, the parameter of main interest in sediment transport studies, but less to retrieve turbidity. However, this parameter has been used as an effective indicator of water quality and, being an optical property, is more tightly related to the backscattering coefficient, b_b in m^{-1}, and thus to reflectance than is *SPM*. Most of the existing works propose site-specific empirical relationships between turbidity and reflectance at different satellite wavebands by fitting field turbidity measurements with either field- or satellite-derived reflectance. Historically, turbidity measurements have been reported in a generic unit such as the Nephelometric Turbidity Unit (NTU), as specified by the United States Environmental Protection Agency (EPA), but it can be also reported in FTU (Formazin Turbidity Unit) and FNU (Formazin Nephelometric Unit) depending on the method and equipment used. All the aforementioned units are based on calibrations using the same primary standard known as Formazin, but in general the use of NTU is limited to instruments that comply with the EPA Method, FNU pertains to instruments that comply with ISO 7027, and FTU when spectrophotometric equipment is used (absorptometric methods) (Anderson, 2006). Unfortunately, turbidity is often reported indistinctly as NTU, FTU or FNU considering all as comparable or equivalent units regardless of the instrument's technology used.

In general, a good correlation is found between turbidity and reflectance at satellite bands located in the red part of the spectrum for low to moderate turbidity values. Landsat band 3 (630–690 nm) has been used to map turbidity in Guadalquivir River (Spain) for a turbidity range 1.5–8 NTU (Bustamante, Pacios, Diaz-Delgado, & Aragonés, 2009). Choubey (1992) found a good correlation between LISS-I red band (620–680 nm) and turbidity in the range of 15–45 NTU in the Tawa reservoir in India. Goodin, Harrington, Druane Nellis, and Rundquist (1996) used SPOT-HRV2 red band (610–680 nm) to map relatively low levels of turbidity, which ranged from 3 to 15 NTU, in the Tuttel Creek reservoir in Kansas, USA. MODIS 250-m resolution band at 645 nm had been successfully used to map turbidity in the Tampa Bay (USA) for turbidities ranging between 0.9–8 NTU (Chen, Muller-Karger, & Hu, 2007). Maltese, Capodici, Ciraolo, and La Loggia (2013) tested and re-calibrated Chen's algorithm for the Sicilian gulfs (Italy) where measured turbidity ranged 1.5–6 FNU. Petus et al. (2010) developed a regional algorithm for MODIS-Aqua 250-m red band to map turbidity in the Adour River plume (Bay of Biscay, France), where field turbidity values varied between 0.5 and 70 NTU. Ouillon et al. (2008) found that the MERIS 681 nm band showed the best fit for turbidity values ranging between 1–25 FTU in three different tropical coastal waters of New Caledonia, Cuba and Fiji. Potes, Costa, and Salgado (2012) found a good linear relationship between turbidity and the ratio between the green (560 nm) and blue (412.5 nm) MERIS spectral bands for turbidity values ranging from 1 to 60 NTU. Conversely, fewer studies have been performed for very turbid waters. A multiple linear regression analysis using Landsat red (630–690 nm) and near-infrared (750–900 nm) bands was used to predict turbidity in a glacial lake in Alaska where highly scattering rock flower (sediment originated from glacial rock weathering) dominates the particulate fraction and where turbidity varied between 2–997 NTU (Liversedge, 2007).

Semi-analytical models have also been proposed for retrieving turbidity. Gohin (2011) derived satellite turbidity from chlorophyll-*a* concentration (Chl-*a*) and non-algal *SPM* concentrations. First, Chl-*a* is determined using pre-defined look-up-tables (Gohin, Druon, & Lampert, 2002), and then non-algal *SPM* is estimated from radiance at 555 nm or 670 nm, depending on the *SPM* level retrieved, by inverting a semi-analytical model (Gohin et al., 2005). Finally, turbidity is derived from Chl-*a* (for the phytoplankton part) and non-algal particles using an empirical relationship between *SPM* and turbidity derived from *in situ* measurements performed in Boulogne and Dunkerque (France) with values ranging from 0.2 to 100 NTU. Nechad et al. (2009) developed a semi-analytical generic one-band algorithm for turbidity as a function of reflectance for coastal waters. The algorithm, which can be used for any optical sensor measuring somewhere in the spectral range 520–885 nm, was calibrated using field radiometric and turbidity measurements from the Southern North Sea (SNS) and validated using an independent set of seaborne measurements from the same region. The algorithm was calibrated for MERIS bands and the best non-linear least-square regression fit between reflectance and turbidity was obtained at the red 681 nm band for turbidity values in the range 0.6–83 FNU.

1.3. Regionality of algorithms

Standard data products from ocean color satellite missions such as MODIS and MERIS are typically based on algorithms which are calibrated and/or validated with *in situ* data for a limited number of regions—see Matthews (2011); and Odermatt, Gitelson, Brando, and Schaepman (2012) for reviews of coastal water ocean color algorithms. The performance of ocean color algorithms outside their calibration/validation regions is a key question. If an algorithm has similar performance in all regions, including those not used in the original algorithm calibration, then it can be considered as a "global" algorithm and can be used with confidence everywhere, even where there is no *in situ* data for validation. If an algorithm performs differently in different regions then it must be considered as a strictly "regional" algorithm and its use outside the calibration regions has greater uncertainty. As regards terminology, the term "region" is not limited here to the geographical sense but could be considered more generically *via* a range of suitably defined parameters, which could be geographical (*e.g.* latitude, longitude), optical (*e.g.* spectral absorption and backscatter coefficients), biogeochemical (*e.g.* suspended particle composition, size distribution and concentration), hydrographic (influence of river discharge, salinity, depth), or others.

In the present study the potential generality of a turbidity retrieval algorithm using the near infrared band at 859 nm band in sediment-dominated waters with moderate to high turbidity is assessed by both analysis of radiative transfer simulations and *in situ* measurements from various coastal and estuarine waters. The radiative transfer simulations cover a wide range of *SPM* concentrations, particulate scattering phase functions (SPFs) and particulate absorption coefficient. In the context of regionality of algorithms, it is important to note the difference between *SPM* retrieval algorithms and turbidity (or backscatter) retrieval algorithms. Turbidity (or backscatter) retrieval algorithms will be sensitive to particle size and type only *via* variability of the SPF. *SPM* retrieval algorithms will be sensitive to particle size and type *via* variability of the SPF but will also be sensitive to variability of other factors such as particle density and refractive index. In other words, since turbidity is, like particulate backscatter, an inherent optical property it is not necessary to consider the potential variability of mass-specific optical properties (Neukermans, Loisel, Mériaux, Astoreca, & McKee, 2012), which are, by contrast, an important source of regional variability for retrieval of *SPM* concentration. For completeness the use of the red 645 nm band in waters with medium to low turbidity is also proposed to ensure that a very wide range of turbidities can be covered.

2. Data and methods

2.1. Remote sensing turbidity algorithm

The semi-empirical single band turbidity (T) retrieval algorithm of Nechad et al. (2009) is analyzed in the present study. It relates turbidity

and marine reflectance at wavelength λ, $\rho_w(\lambda)$, which is defined as $\pi L_w(\lambda) / E_d^{0+}(\lambda)$, where L_w is the water-leaving radiance and E_d^{0+} is the above-water downwelling irradiance, through

$$T = \frac{A_T^{\lambda}\rho_w(\lambda)}{\left(1-\rho_w(\lambda)/C^{\lambda}\right)} \quad [\mathrm{FNU}] \tag{1}$$

where A_T and C are two wavelength-dependent calibration coefficients. A complete list of symbols is provided in Table 1. The parameter C was calibrated using "standard" inherent optical properties (IOPs) as described in Nechad, Ruddick, and Park (2010), while the A_T coefficient was obtained by a non-linear least-square regression analysis using *in situ* measurements of T and ρ_w (see Appendix A for a detailed algorithm description). The A_T^{645} coefficient was derived using *in situ* data obtained in the Southern North Sea (cruises performed between 2007–2010), while A_T^{859} was calibrated using data with T ranging from 10 to 255 FNU from the above mentioned Southern North Sea cruises and two campaigns in the Scheldt estuary (SC) performed in 2010 (Dogliotti et al., 2011). The coefficients at the two wavelengths are given in Table 2.

In the present work we focus the analysis on the algorithm using the 859 nm band for medium to high turbidity values. At this wavelength the high pure water absorption (~4.4 m^{-1}, Kou, Labrie, & Chylek, 1993) avoids saturation of the algorithm expected at lower wavelengths (Bowers, Boudjelas, & Harker, 1998). However, to cover the wider range of turbidities that can be found in coastal waters and to avoid the expected reduced sensitivity of this band at low turbidity, the use of the red band at 645 nm is also proposed. An analysis of the field data used to calibrate the algorithm at the two wavelengths, *i.e.* from SNS (2007–2010) and SC (2010), showed that for $\rho_w(645)$ values lower than 0.05 (corresponding to modeled $T \sim 15$ FNU) there is a good agreement between field and modeled T (Fig. 1). At higher reflectance values, the model sensitivity decreases as one moves away from the linear regime and approaches the saturation region. Thus, an algorithm scheme based on variable bands, as in Shen, Verhoef, Zhou, Salama, and Liu (2010), is suggested based on the reflectance value at 645 nm. In order to assure a smooth transition between the two algorithms, a linear weighting function (between 0 and 1) is applied to the modeled T for $\rho_w(645)$ ranging between 0.05 and 0.07. In summary, we use the 645 nm band when $\rho_w(645) < 0.05$, the 859 nm band when $\rho_w(645) > 0.07$ and blend the two algorithms when $0.05 < \rho_w(645) < 0.07$. In the transition zone, the weight of the algorithm (w) changes linearly from 0 at $\rho_w(645) = 0.05$ to 1 at $\rho_w(645) = 0.07$. Thus, blending is done according to the following formula: $T = (1 - w) \cdot T_{645} + w \cdot T_{859}$, where T_{645} is the turbidity calculated using the 645 mn band and T_{859} is the turbidity calculated using the 859 mn band in Eq. (1).

Table 1
List of symbols and notations.

Symbol	Description	Unit
β	Volume Scattering Function (VSF)	m^{-1} sr^{-1}
ϕ	Relative azimuth angle between the sun and sensor	Degrees
γ_c	Spectral slope of the particulate beam attenuation spectrum	–
λ	Wavelength	nm
ρ_w	Water reflectance	–
θ_s	Sun zenith angles	Degrees
θ_v	Viewing zenith angle	Degrees
χ	Scattering angle	Degrees
a_{CDOM}	Colored dissolved organic matter absorption coefficient	m^{-1}
a_{np}	Non-particle absorption coefficient	m^{-1}
a_p	Particle absorption coefficient	m^{-1}
a^*_p	Mass-specific particle absorption coefficient	m^2 g^{-1}
a^*_{pT}	Turbidity-specific particulate absorption coefficient	m^{-1} FNU^{-1}
b_{90p}	Particle side-scattering coefficient (scattering at 90°)	m^{-1}
b_b	Total backscattering coefficient	m^{-1}
b_{bp}	Particulate backscattering coefficient	m^{-1}
b^*_{bpT}	Turbidity-specific particulate backscattering coefficient	m^{-1} FNU^{-1}
b_p	Particulate scattering coefficient	m^{-1}
b^*_p	Mass-specific particulate backscattering coefficient	m^2 g^{-1}
c^*_p	Mass-specific particulate beam attenuation coefficient	m^2 g^{-1}
Chl-*a*	Chlorophyll-*a* concentration	mg m^{-3}
E_d^{0+}	Above-water downwelling irradiance	W m^{-2} nm^{-1}
L_w	Water-leaving radiance	W m^{-2} sr^{-1} nm^{-1}
S	Spectral slope of the particulate absorption spectrum	nm^{-1}
SPF	Scattering phase function	sr^{-1}
SPM	Suspended particulate matter	g m^{-3}
T	Turbidity	FNU

Table 2
Calibration coefficients C and A_T (FNU) for the 645 nm and 859 nm MODIS bands taken from Nechad et al. (2010) and Dogliotti et al. (2011).

λ (nm)	A_T	C_T
645	228.1	0.1641
859	3078.9	0.2112

2.2. Field measurements

New *in situ* measurements were collected from various European and South American coastal and shallow estuarine environments characterized by high concentrations of suspended sediments and a variety of environmental conditions (Fig. 2, Table 3). This dataset was not used to derive or calibrate the algorithm of Section 2.1. Data from the southern North Sea (SNS) were collected during a cruise onboard the *Belgica* research vessel in 2011, primarily in Belgian coastal waters. This region is a relatively shallow area (<50 m) subject to strong vertical mixing from strong winds and tidal currents (Ruddick & Lacroix, 2006) where sediment resuspension causes relatively high *SPM* concentrations (~1–200 g m^{-3}).

Measurements from the Scheldt (SC) estuary were collected from a fixed pontoon (51°14′ N–4°23′ E) located near the city of Antwerp (Belgium) in June 2012 and October 2013. The Scheldt is a relatively turbid estuary where *SPM* values can reach up to 400 g m^{-3} and are subject to strong tidal and seasonal variations (Arndt, Vanderborght, & Regnier, 2007).

Data from the Gironde (GIR) estuary were collected from two fixed pontoons located in Pauillac (45°11.83′ N–0°44.58′ W) and Blaye (45°7.51′ N–0°40.03′ W) in southwest France in June 2012 and August 2013. This macrotidal estuary is characterized by highly turbid waters dominated by suspended sediments. Mean *SPM* concentrations vary from 150 to approximately 3000 g m^{-3} in surface waters (Allen, Salomon, Bassoullet, Du. Penhoat, & Degranpré, 1980).

Measurements from Río de la Plata (RdP) were performed from a fixed pontoon at the Palermo Fishermen Pier (34°20.18′ S–58° 14.36′ W) located in Buenos Aires (Argentina) in November 2012. The city is located in the upper part of the estuary where it is very shallow (<5 m). The river carries a large amount of suspended particulate and dissolved organic matter and high values of *SPM* have been reported in this region, with mean values ranging from 100 to 300 g m^{-3} and extreme concentrations up to 400 g m^{-3} (C.A.R.P., 1989; Urien, 1967).

A field campaign was performed in the turbid coastal waters of French Guyana (FG) in October 2009. The sampled area is located in relatively shallow waters which are strongly influenced by the Amazon River discharge and characterized by mudflats all along the coast (Froidefond, Lahet, Doxaran, Prost, & Ternon, 2004; Loisel et al., 2009). Optical properties in these waters have been shown to be mainly driven by mineral particles of terrestrial origin (Loisel et al., 2009).

Water samples were collected from the surface and turbidity was measured using portable HACH 2100P and 2100QIS turbidimeters as in Nechad et al. (2009). The instrument records turbidity between 0 and 1000 FNU, with a resolution of three significant figures. A 10-ml vial containing the water sample is illuminated by a light-emitting diode with emission at 860 ± 60 nm. The instrument measures turbidity *via* the ratio of light scattered at an angle of 90° ± 2.5° to forward-

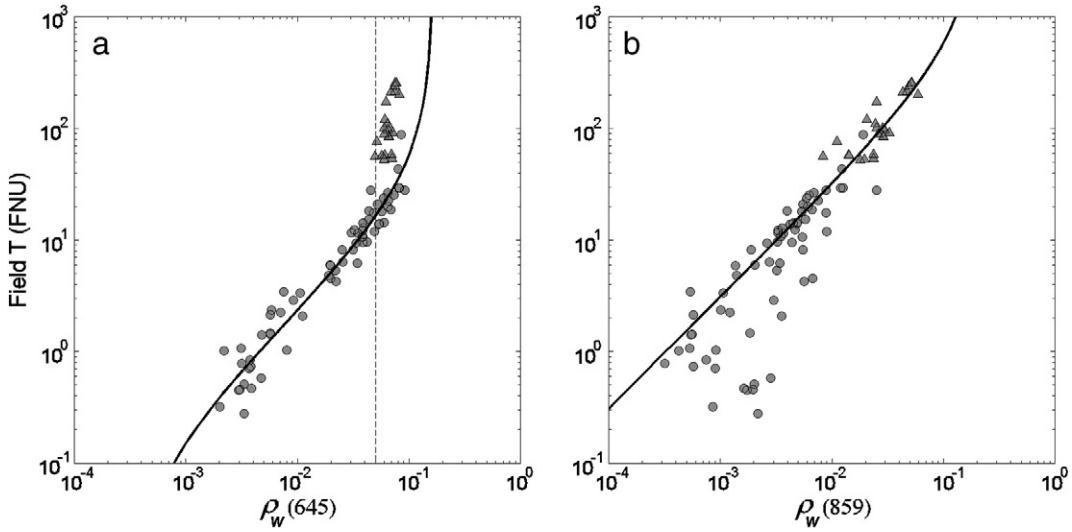


Fig. 1. Scatter plot of field T (FNU) *versus* a) $\rho_w(645)$ and b) $\rho_w(859)$ for measurements performed in the Southern North Sea in 2007–2010 (circles, N = 66) and Scheldt estuary in 2010 (triangles, N = 23) used to calibrate the algorithms. The black line is the semi-analytical model (Eq. 1) for each wavelength. The vertical dash line shows $\rho_w(645) = 0.05$.

transmitted light as compared to the same ratio for a standard suspension of Formazin. This optical measurement technique of turbidity from the side-scattering coefficient, b_{90}, is in accordance with ISO 7027 (1999), and determines turbidity in Formazin Nephelometric Unit (FNU). Turbidity was recorded in triplicates that were averaged. Turbidities of the STABLCAL Stabilized Formazin Turbidity 10 or 20, 100 and 800 FNU standards and that of pure water were recorded after each sampling campaign to check the instrument stability.

Above-water marine reflectance measurements were collected with a set of three Trios-RAMSES hyperspectral radiometers with a sampling interval of approximately 3.3 nm and an effective spectral resolution of about 10 nm covering the spectral range 400–900 nm. The protocol described in Ruddick, De Cauwer, Park, and Moore (2006) was followed except that a) for measurements from fixed structures the standard viewing azimuth of 135° relative to sun was modified to 90° when necessary to minimize structure perturbations of the light field, and b) for measurements in estuaries with fetch-limited surface waves the wind speed was set to zero in estimation of the Fresnel reflectance. The hyperspectral reflectance data were integrated over the relative spectral response function of MODIS band 2 to obtain $\rho_w(645)$ and $\rho_w(859)$.

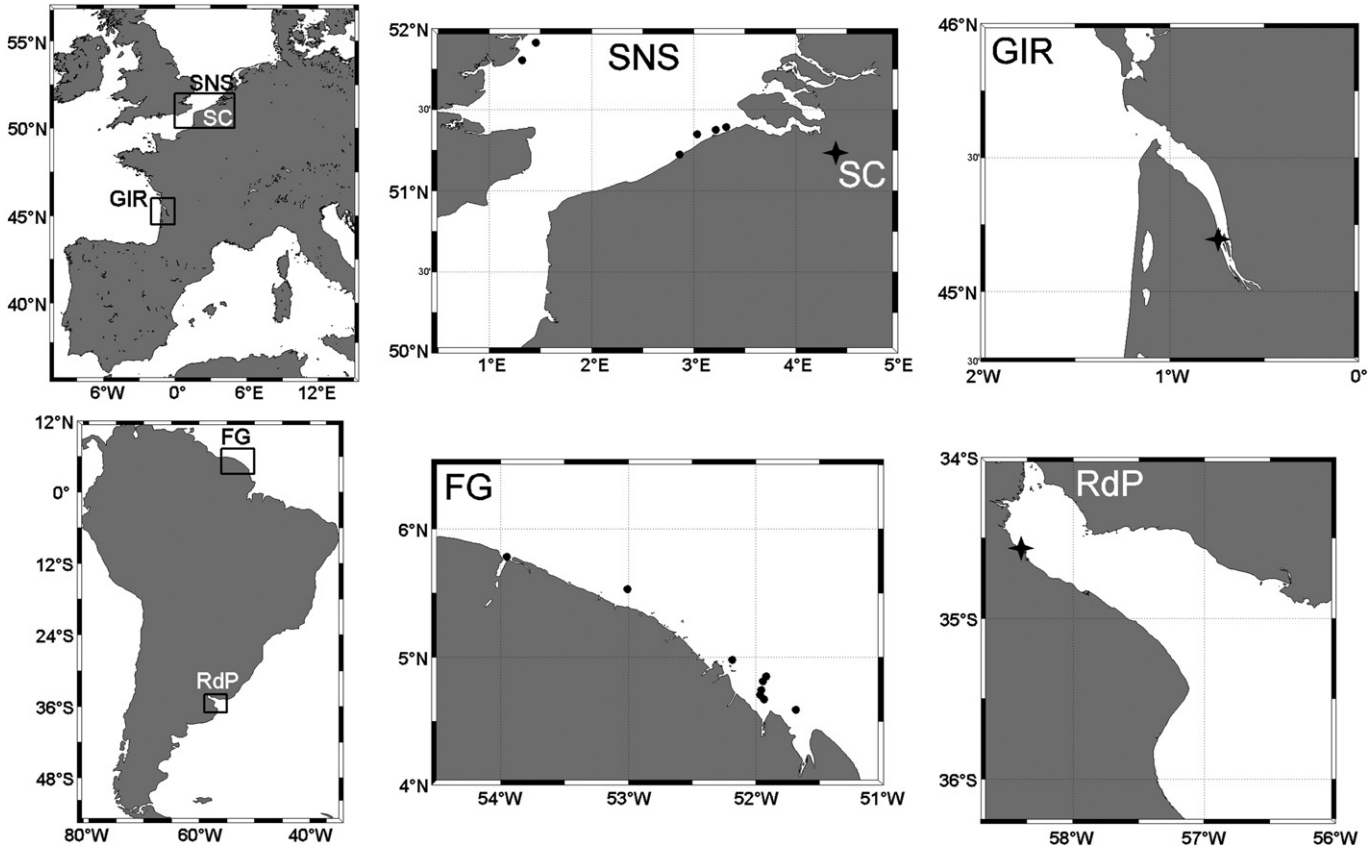


Fig. 2. Location of stations sampled during oceanographic campaigns in Southern North Sea (SNS) and French Guyana (FG), and fixed stations in the Scheldt (SC), Gironde (GIR), and Río de la Plata (RdP) estuaries.

Table 3
Summary of sites, platforms, date of sampling, mean position, and conditions for measurements (temperature, salinity and sun zenith angle (SZA), with median and [minimum–maximum] values). NA: not available.

Location	Platform	Time period	Latitude	Longitude	Temperature [°C]	Salinity [PSU]	SZA [°]
Southern North Sea	Belgica R/V	4–7 Jul 2011	51° 23.14′ N	02° 50.00′ E	18.5 [17.8–19.2]	33.4 [31.8–34.4]	38.2 [28.7–60.7]
French Guyana	Papi Jo R/V	13–17 Oct 2009	04° 44.57′ N	52° 10.80′ W	NA	NA	36.4 [14.4–57.2]
Scheldt	St. Anna pontoon	2 & 5 Jun 2012	51° 14.05′ N	04° 23.78′ E	18.7	5.0 [1.1–6.4]	35.4 [28.6–49.8]
		1 Oct 2013			NA	NA	55.2 [54.6–56.5]
Gironde	Pauillac pontoon	15–16 Jun 2012	45° 11.83′ N	00° 44.58′ W	20.7 [20.5–21]	1.9 [1.6–3.0]	43.9 [21.9–74.5]
	Blaye pontoon	12–16 Aug 2013	45° 07.52′ N	00° 40.03′ W	NA	NA	39.9 [30.9–55.1]
Río de la Plata	Fishermen Pier	14–23 Nov 2012	34° 33.65′ S	58° 23.93′ W	25.4 [22.9–27]	0.16 [0.02–0.18]	31.2 [14.3–74.8]

For the present analysis the quality control criteria retained only marine reflectances that were collected in homogeneous sunny skies (as indicated by the relation $L_{sky}^{0+}/E_d^{0+}(750) < 0.05\ sr^{-1}$, where L_{sky}^{0+} is the measured sky radiance), and with small deviation from the time-averaged mean reflectance at 859 nm and 645 nm, *i.e.* a coefficient of variation (standard deviation to mean ratio) CV < 20%. After applying the quality control, the number of field measurements used to evaluate the algorithms was 8 for SNS and SC, 9 for FG, 40 for RdP, and 41 for GIR, totalizing 106 measurements considering all sites together (see Table 4).

2.3. Radiative transfer simulations

Radiative transfer simulations were performed using Hydrolight 5.0 (Mobley & Sundman, 2008) at a single wavelength (859 nm) considering only water and mineral particles, *i.e.* colored-dissolved organic matter (CDOM) absorption and chlorophyll-*a* concentration were set to zero. Absorption and scattering for water were taken from Kou et al. (1993) and Morel (1974), respectively. Water absorption is so high in the near infrared (~4.4 m^{-1} at 859 nm) that light absorption by phytoplankton and CDOM can be assumed negligible in comparison (Babin & Stramski, 2002). Simulations were performed for mineral particle concentrations that varied from 0.1 to 1000 g m^{-3}. Fournier–Forand (FF) scattering phase functions (SPFs) with four different backscattering ratios (b_{bp}/b_p) were used (0.01, 0.0183, 0.03, and 0.05). These values cover the extreme range of values reported in the literature for coastal waters dominated by non-algal particulate matter which varied between 0.01 and 0.06, with a mean value of approximately 0.02 (*e.g.* Boss et al., 2004; Chami, McKee, Leymarie, & Khomenko, 2006; Loisel, Mériaux, Berthon, & Poteau, 2007; McKee et al., 2009; Snyder et al., 2008; Tzortziou et al., 2006; Whitmire, Boss, Cowles, & Pegau, 2007). For each SPF, the particle backscatter to absorption ratio (b_{bp}/a_p) was obtained by varying both b_{bp} and a_p. The mass-specific particulate absorption, $a_p^*(\lambda)$, was extrapolated from 443 nm using

$$a_p^*(\lambda) = a_p^*(443) \times \exp\left[-S(\lambda - 443)\right] \quad (2)$$

where $a_p^*(443) = 0.041\ m^2\ g^{-1}$ and the spectral slope $S = 0.0123\ nm^{-1}$ are taken from Babin, Stramski, et al. (2003). The equation was originally developed for the 380–730 nm range and is assumed to be valid beyond 730 nm. Mass-specific particulate scattering, $b_p^*(\lambda)$, was obtained using Eq. (2) and modeling the mass-specific particulate beam attenuation, $c_p^*(\lambda)$, as

$$c_p^*(\lambda) = \left[a_p^*(555) + b_p^*(555)\right] \times (\lambda/555)^{-\gamma_c} \quad (3)$$

where $b_p^*(555) = 0.51\ m^2\ g^{-1}$ and the spectral slope of the beam attenuation $\gamma_c = 0.3749$ were taken from Babin, Morel, Fournier-Sicre, Fell, and Stramski (2003). The water was modeled as homogeneous and infinitely deep. Surface downwelling light was modeled for sun zenith angles (θ_s) varying from 0° to 60°, a nominal wind speed of 5 m s^{-1}, clear and overcast sky conditions were considered, and the surface irradiance was calculated using the RADTRANX model supplied as part of the Hydrolight code. The particle side-scattering coefficient, b_{90p}, is defined here as $2\pi * \beta_p(90°)$ where $\beta(\chi)$ is the Volume Scattering Function (VSF) for scattering angle χ as defined in Mobley, Sundman, and Boss (2002). With this definition a VSF which is independent of angle in the backscattering directions, *i.e.* with $\beta(\chi) = \beta(90°)$ for $\chi > 90°$, has equal side- and backscattering coefficients. For the four SPFs defined above (FF = 0.01, 0.0183, 0.03, and 0.05) the ratio of b_{90p}/b_{bp} is 1.47, 1.44, 1.38, and 1.31, respectively.

Table 4
Equation and statistics of the linear regressions between modeled and field T [FNU] measurements for each site and all sites together: r (dimensionless), *RMSE* (FNU), ε (%), and δ (%). Only $T < 1000$ FNU were considered.

	Slope	*Intercept*	*r*	*RMSE*	*ε*	*δ*	*n*	*T-range*
SNS	0.84	−0.13	0.99	5.1	21.8	−11.9	8	1.8–84
SC	0.97	−15.22	0.97	22.3	13.3	−13.3	8	103–250
GIR	1.05	6.00	0.94	32.8	14.7	6.7	41	41–988
FG	1.18	−5.51	0.99	28.1	11.8	8.2	9	11–490
RdP	0.93	14.10	0.83	7.9	11.6	9.1	40	62–185
All	1.07	−1.29	0.97	20.5	13.7	4.8	106	1.8–988

3. Results

3.1. Sensitivity of the 859 nm algorithm to different factors

3.1.1. Scattering phase function

Natural variability of the SPF is an important potential source of uncertainty for turbidity estimation from Eq. (1), which assumes a single SPF. The radiative transfer simulations are here analyzed to estimate this uncertainty at 859 nm. The results are presented both in terms of side-scattering, directly relevant for turbidity, and in terms of backscattering because the latter is used in analytical reflectance models including the first order model of Gordon et al. (1988) used by Nechad et al. (2010) to derive Eq. (1).

Simulations performed for a large range of particle concentrations (0.1–1000 g m^{-3}) for four different SPFs using particle-backscattering ratios typically found in coastal waters showed that lower variability in retrieved b_{90p} is expected due to varying SPFs compared to b_{bp}, especially for the more turbid cases, *i.e.* higher reflectance (Fig. 3a–b). In Fig. 3a–b this is illustrated for the case of $\rho_w(859) = 0.1$, showing as "SPF-related uncertainty" (ΔSPF) the range of possible retrieved b_p, b_{90p} or b_{bp} for the different possible SPFs, which is unknown in the retrieval context. The influence of varying SPFs is much more significant for b_p (Fig. 3c), indicating that retrieval of b_p, unlike b_{90p} or b_{bp}, will have high uncertainty associated with natural variability of the SPF.

This SPF-related uncertainty is further analyzed by quantifying the range of side-, back- and total scattering coefficients that correspond to the same reflectance when different SPFs are considered. Thus, Fig. 4 shows the change in side-, back- and total scattering coefficients that are needed to give the same reflectance as a reference SPF ($b_{bp}/b_p = 0.0183$ hereafter referred as FF = 0.0183) when the SPF is varied over a range of SPF typically found in coastal waters, given by backscattering ratios of 0.01 and 0.03 (referred as FF = 0.01 and

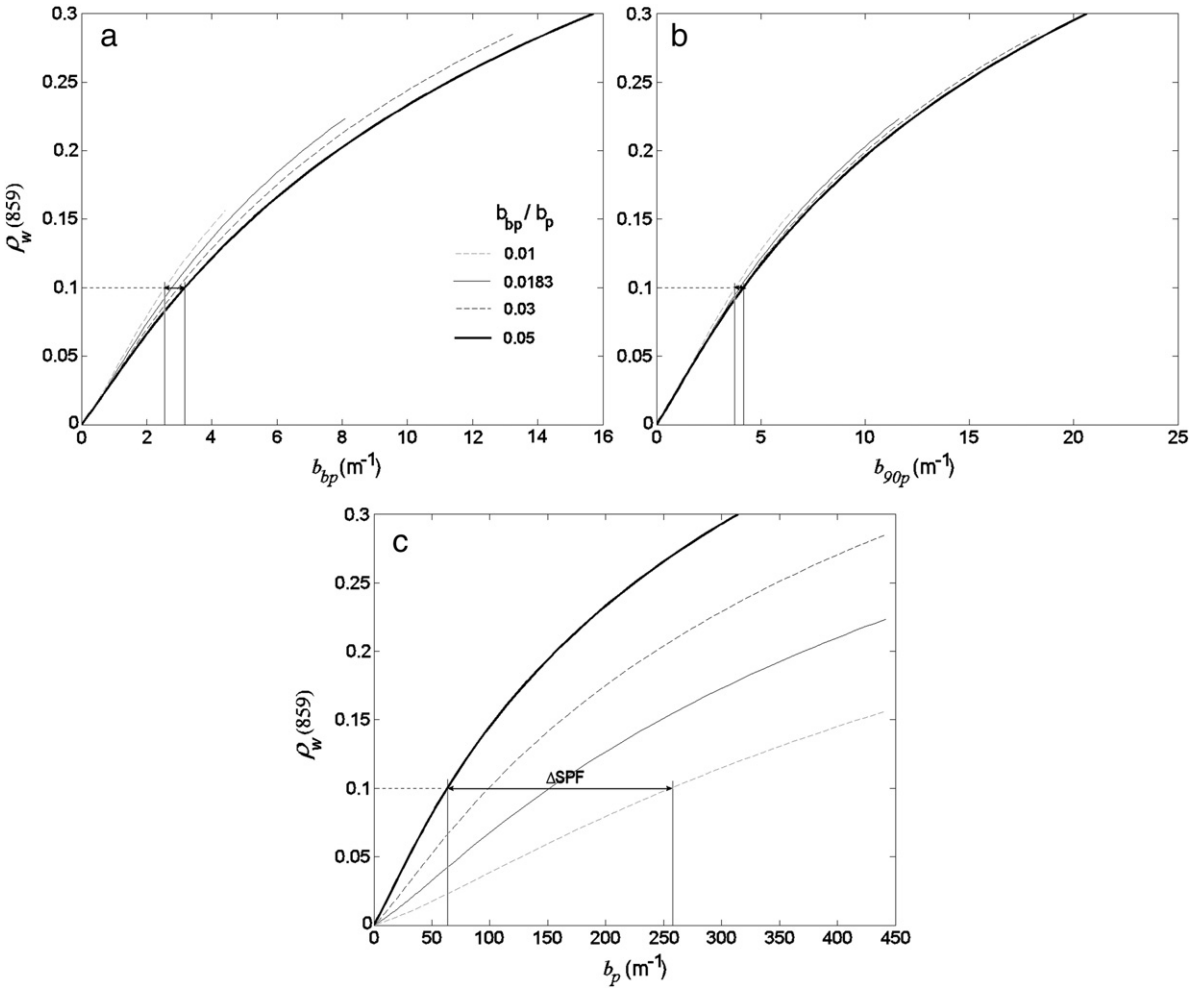


Fig. 3. Reflectance at 859 nm as a function of a) b_{bp}, b) b_{90p}, and c) b_p for various SPFs defined by the b_{bp}/b_p ratio. As an example, the SPF-related uncertainty (ΔSPF), *i.e.* the range of possible retrieved b_{bp}, b_{90p}, and b_p, for $\rho_w(859) = 0.1$ is indicated by the vertical lines in each case.

FF = 0.03). This represents directly an important component of retrieval algorithm uncertainty since the SPF is generally not known *a priori*. The total scattering coefficient, as was previously observed in Fig. 3, shows the highest variability (bold lines in Fig. 4a) and thus greatest sensitivity to SPF variations over the whole reflectance range. This can be explained by the fact that b_p integrates all scattering angles including forward scattering angles, whereas reflectance is almost insensitive to near-forward scattering. Uncertainty on b_p varied from 35 and 40% for FF = 0.03 and up to 70 and 85% for FF = 0.01 (bold lines in Fig. 4a), both increasing at lower reflectance values. At high reflectance,

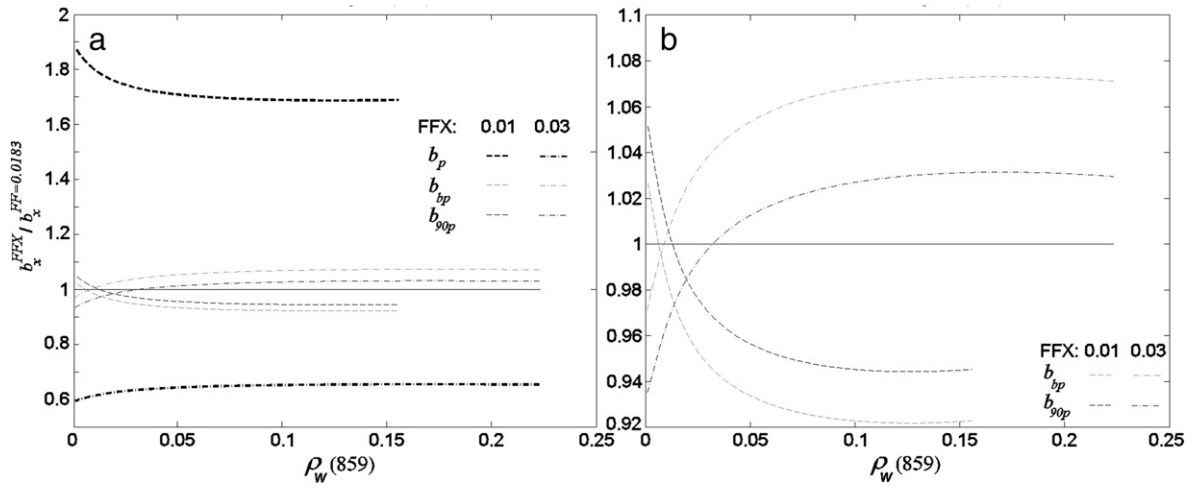


Fig. 4. a) Total particle scattering (b_p, bold black lines), back-scattering (b_{bp}, gray lines) and side-scattering (b_{90p}, black lines) for FF = 0.01 (dashed lines) and FF = 0.03 (dot-dashed lines) normalized to the corresponding scattering for FF = 0.0183 as a function of reflectance at 859 nm. Nadir viewing, $\theta_s = 30°$, and clear sky condition were used here. b) Same as a) but only b_{90p} and b_{bp} are considered.

side-scattering is less sensitive to varying SPFs: uncertainty in b_{90p} reached up to 6% for FF = 0.03 and 5% for FF = 0.01 (black lines in Fig. 4), while b_{bp} varied up to 7.5% for FF = 0.03 and 8% for FF = 0.01 (gray lines in Fig. 4). At high reflectance, multiple forward scattering and side scattering influence more the reflectance than the larger scattering angles do. In turn, at low reflectance b_{90p} is more sensitive to SPF up to 5 and 6%, compared to b_{bp} (up to 2%) given that in a quasi-single scattering regime light scattered at high scattering angles is better represented by b_{bp} than by b_{90p}.

3.1.2. Bidirectional effects

To assess the turbidity algorithm uncertainty due to bidirectional distribution of sea water reflectance at 859 nm, the side-scattering was computed for different viewing geometries and illumination conditions given a fixed SPF (*e.g.* FF = 0.0183) (Fig. 5). Three viewing geometries, given by viewing zenith angle (θ_v) and relative azimuth angle between the sun and sensor (ϕ), were selected: i) $\theta_v = 40°$ and $\phi = 135°$, ii) $\theta_v = 40°$ and $\phi = 90°$, and iii) Nadir viewing, *i.e.* $\theta_v = \phi = 0°$. The first two are typical above-water radiometry viewing geometries, as used for the calibration dataset. Three sun zenith angles (θ_s) were also analyzed: 1) $\theta_s = 0°$ (at zenith), 2) $\theta_s = 30°$ and 3) $\theta_s = 60°$ for clear and overcast skies. The results show that uncertainty is sensitive to varying viewing geometry (up to 7%) and, to a less extent, to illuminating conditions, reaching up to 3.5% (Fig. 5a and b, respectively).

3.1.3. Other factors

In order to quantify the uncertainty in the turbidity retrieval at 859 nm due to natural variability of b_{bp}/a_p, which is related to the particle type, additional simulations were performed for varying parameters that were previously fixed in Eqs. (2) and (3), *i.e.* the mass-specific particulate absorption and backscattering coefficients (a_p^* (443) and b_p^* (555)) and absorption and attenuation spectral slopes (S and γ_c), as well as different SPFs. Simulations were performed using values taken from previously published studies, *i.e.* a_p^* (443) ranging between 0.018 and 0.064 $m^2\ g^{-1}$ and S varying from 0.011 to 0.0136 nm^{-1}, to cover the variability found in coastal waters reported in Babin, Stramski, et al. (2003), b_p^* (555) ranged between 0.1 and 0.8 $m^2\ g^{-1}$ (Babin, Morel, et al., 2003), and γ_c from 0.3 to 1.15 to cover the variability found by Boss et al. (2001) in waters dominated by detritus and resuspended sediments. As previously (Figs. 4 and 5), uncertainty in the retrieved b_{90p} was calculated by normalizing the values to a reference value for a given combination of input variables. In this case typical mean values found in coastal waters such as $b_{bp}/b_p = 0.0183$, a_p^* (443) = 0.041 $m^2\ g^{-1}$, $S = 0.0123\ nm^{-1}$, b_p^* (555) = 0.51 $m^2\ g^{-1}$, and $\gamma_c = 0.3749$ were chosen. Results show that uncertainty can be up to 10% and 15% at high and low reflectance, respectively, when b_{bp}/a_p ranges over one order of magnitude (Fig. 6).

In coastal waters where terrestrial inputs are important CDOM absorption in the blue part of the spectrum can be very high (up to 90% of the total absorption). However, it decreases exponentially with increasing wavelength (Bricaud, Morel, & Prieur, 1981), being very low in the NIR compared to water absorption. When considering relatively high CDOM absorption values at 443 nm, *e.g.* a_{CDOM} (443) ranging from 0.1 to 0.7 m^{-1} and mean slope of 0.0176 nm^{-1} typically found in coastal areas with terrestrial origin (Babin, Stramski, et al., 2003), CDOM absorption in the NIR (859 nm) varies between 6.6 10^{-5} and 4.6 10^{-4} m^{-1}. Considering that water absorption in the NIR is relatively high (4.4 m^{-1}), CDOM absorption is only 0.0015 to 0.0105% of the water absorption, reaching up to 0.034% when natural variability in the CDOM absorption spectral slope is considered (Babin, Stramski, et al., 2003). Thus, CDOM absorption, generally high in turbid estuaries, will have negligible influence in the turbidity retrieval algorithm for sediment-dominated waters using NIR bands.

Another source of uncertainty is related to the variability of water absorption with temperature and salinity. Using the Water Optical Properties Processor (WOPP), a computer program to calculate the inherent optical properties (IOPs) of pure water at a specific water temperature and salinity, Röttgers et al. (2012) found that the relative change in water absorption is −0.027% per °C and −0.009% per PSU (Practical Salinity Unit) for the OLCI NIR band at 866 nm. Thus, in this NIR band the impact on reflectance comes mainly from the uncertainty of the temperature effect. At low reflectance variability of water absorption due to a change from 0 to 20 °C would cause an uncertainty in reflectance of 0.5%, while at high reflectance the impact would be less and could be considered negligible.

3.2. Algorithm performance in different regions

The one-band algorithm (Eq. 1) using 645 nm and 859 nm bands and the switching scheme presented above was applied to reflectance measured at five different locations, covering a variety of suspended particles in terms of turbidity range, composition, size distribution, and refractive index. The dataset used here to evaluate the algorithm is independent of the dataset used for the algorithm development and calibration. To evaluate the algorithm performance, statistics of the linear regression (*slope*, *intercept*, *root-mean-square error*, *RMSE*) between

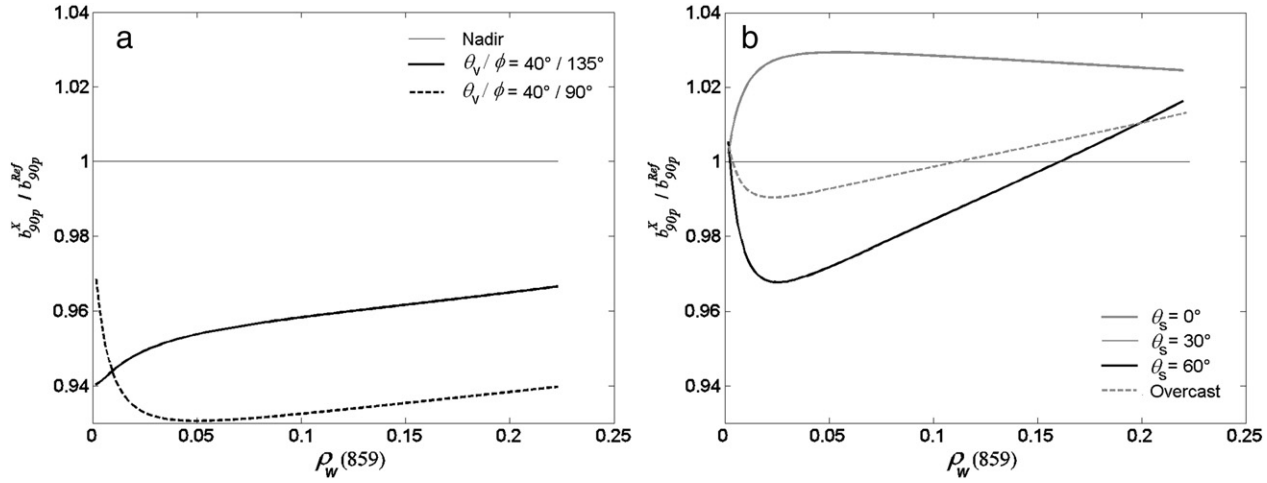


Fig. 5. Particle side-scattering (b_{90p}) normalized to b_{90p} at a reference condition (b_{90p}^{Ref}): Nadir viewing, $\theta_s = 30°$, and FF = 0.0183 for variable: a) observation geometries (θ_v and ϕ), and b) illuminating conditions (θ_s for clear and overcast skies).

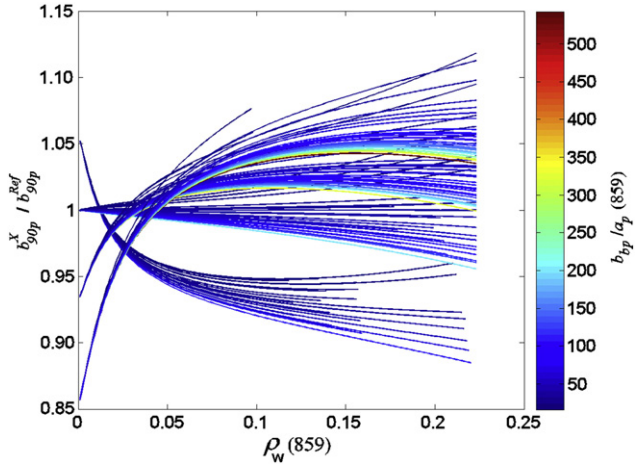


Fig. 6. Side-scattering for variable b_{bp}/a_p ratio normalized to a reference value obtained using a combination of typical mean values found in coastal waters for SPF, SIOPs, and absorption and attenuation spectral slopes (see text in Section 3.1.3 for values).

modeled (T_{mod}) and field (T_{field}) values were calculated. In order to evaluate the uncertainty, the mean absolute relative percentage error (ε) and bias (δ) were calculated as

$$\varepsilon = \frac{1}{n}\sum \frac{|T_{mod} - T_{field}|}{T_{field}} \times 100 \quad (4)$$

$$\delta = \frac{1}{n}\sum \frac{T_{mod} - T_{field}}{T_{field}} \times 100 \quad (5)$$

where n is the number of observations. The correlation between modeled and field measurements (r) was also computed (Table 4).

Comparisons showed a general good agreement between field and modeled T for all the sites analyzed. Reflectance increased with increasing T up to ~20 FNU for $\rho_w(645)$ and up to ~1000 FNU for $\rho_w(859)$, and then tended to saturate at higher values, respectively (Fig. 7). A good performance of the algorithm using the 645 nm band for low T can be observed for both the SNS and FG datasets (solid symbols in Fig. 7a). In Fig. 7 solid symbols indicate when the 645 nm and 859 nm band algorithm is used, while empty symbols show when the weighted combination between the two algorithms is used. The portable HACH turbidimeter measures T values up to 1000 FNU, so dilutions were performed with MilliQ water at four stations for which readings exceeded this limit in the Gironde estuary. Even though dilution might change the particle size distribution thus contaminating the measurement, a good agreement with field data was still found for these samples (Fig. 7b). In order to avoid the asymptotic regime where saturation occurs and T retrieval is less reliable, statistical analysis was performed for $T < 1000$ FNU. Equations and statistics of the regressions for each region and considering the entire data base are shown in Table 4. Scatter plot of modeled (using the switching one-band algorithm) *vs.* field T is shown in Fig. 8. A good correlation between modeled and field values was observed for each site with a correlation coefficient $r > 0.9$ at all sites except for RdP ($r = 0.83$). On average, T was underestimated by ~12% in SNS and SC and overestimated between 7% and 9% in the GIR, RdP and FG. Mean relative errors ranged between 11 and 15% in FG, RdP, SC and GIR, and were highest in SNS (ε ~ 22%). Slopes of the linear regressions were close to 1, and *RMSE* ranged between 5 (SNS) and 33 FNU (GIR). When the entire data base was considered ($n = 106$), a general good performance of the algorithm was found with a correlation coefficient $r = 0.97$, relatively small bias (4.8%), and a mean relative error of ~14%. The fitted linear regression explained 97% of the variability with a slope close to 1 (1.07), intercept close to zero (−1.29) and *RMSE* of 20.5 FNU (Table 4).

4. Discussion

4.1. Generality of the 859 nm band algorithm

The single band turbidity algorithm analyzed in the present study (Dogliotti et al., 2011; Nechad et al., 2009) was derived assuming a constant T-specific particulate backscattering coefficient (b_{bp}/T). Since T is an optical property (side-scattering), the variability of the side to backscattering ratio is expected to be lower than, for example, the *SPM*-specific backscattering coefficient (b_{bp}/SPM) which has been shown to vary by a factor of 3 or 4 and depends on the particle composition *i.e.* organic- or inorganic-dominated waters (Doxaran et al., 2012; Loisel et al., 2009; Martinez-Vicente, Land, Tilstone, Widdicombe, & Fishwick, 2010; Neukermans et al., 2012). In general, less *in situ* measurements of concomitant T and b_{bp} have been performed compared to *SPM* and b_{bp} values. Neukermans (2012) estimated the variability of $\beta_p(120°,658\ nm)/\beta_p(90°,658\ nm)$ to be within a factor of 1.7 with a mean value of 1.2 using *in situ* VSF measurements carried out in a wide range of water types using the Wetlabs MASCOT instrument

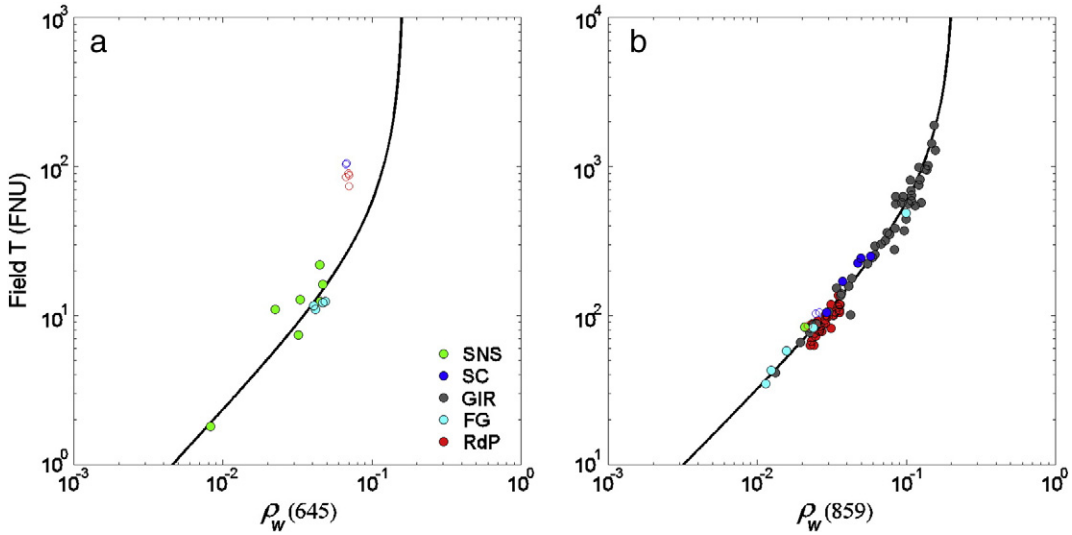


Fig. 7. Scatter plot of field T (FNU) *versus* a) $\rho_w(645)$ and b) $\rho_w(859)$. Measurements performed in SNS, SC, GIR, FG, and RdP are shown in different colors. The black line is the semi-analytical model for each wavelength and solid symbols indicate when the corresponding algorithm is used, while empty symbols indicate when a weighted combination between the two algorithms is used.

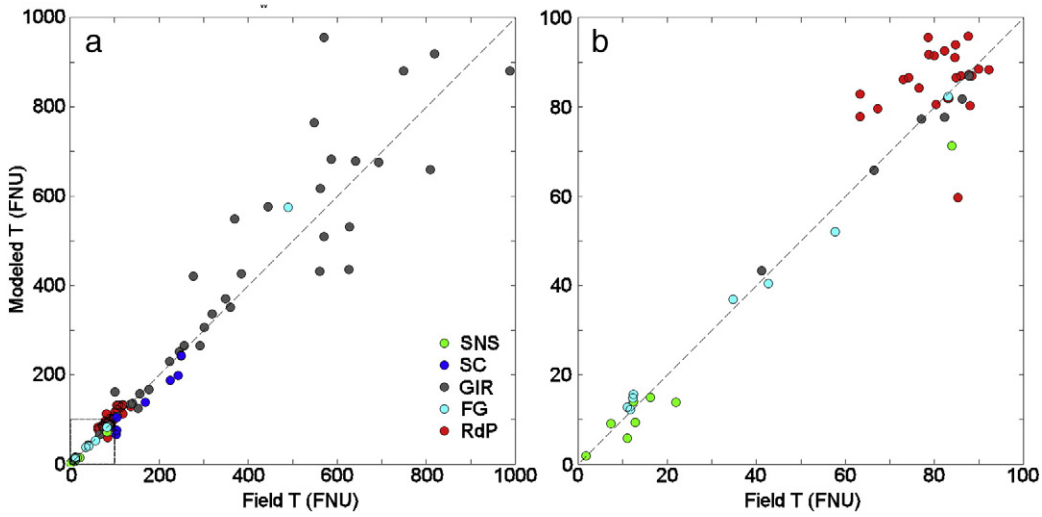


Fig. 8. a) Scatter plot of modeled *versus* field *T* (FNU) measurements performed in SNS, SC, GIR, FG, and RdP. b) Detail of the scatter plot at low *T* range (0–100 FNU). The dashed line is the 1:1.

(Sullivan & Twardowski, 2009). The SPFs used in this study have a b_{bp}/b_{90p} ratio at 859 nm that varies by a factor of 1.2. However, it is interesting to note that the SPF-related retrieval uncertainty for b_{90p} can be less than that for b_{bp} suggesting that the *T* retrieval algorithm in Nechad et al. (2009), which uses a b_{bp}-based reflectance model and assumes a constant b_{bp}/T ratio, could be replaced by a reflectance model based directly on *T*.

Variability in measured *T* may result from differences in the turbidimeter design and technology used. Different methodologies and instruments exist to measure turbidity involving different types of light sources (*e.g.* white light and infrared light, tungsten and light emitting diode (LED) lamps) and detector arrangements. Inter-comparisons between turbidimeters with different designs and technologies have been performed. Low variations were found when Formazin standards were compared (2–7%, Barter & Deas, 2003), but higher variability was found for natural samples, ranging from 7–44% (Barter & Deas, 2003) and between 12–100% (Lewis, Eads, & Klein, 2007). A high variability (*i.e.* a factor of 2) was found in the relation between b_{bp} and turbidity when measured using an instrument with a wide solid angle like the Seapoint turbidity meter, *i.e.* integrating the particulate VSF between 15° and 150° at 880 nm (Neukermans, 2012). Conversely, in this study during RdP and GIR campaigns four HACH 2100P and 2100QIS portable turbidimeters (with same technology and design) have been used and inter-instrument comparisons showed a low variability for Formazin standards, with CV varying between 0.2 and 3%, while for natural samples the variability was 0.5–5.9% (RdP) and 0.4–5.9% (GIR).

The sensitivity analysis performed using radiative transfer simulations, which covered a wide range of natural conditions, showed that uncertainty in the retrieved turbidity can reach up to 6% when variable SPF and mean specific inherent optical properties (SIOPs) were considered. However, when natural variability of SIOPs was considered, higher values were found (up 10%). It should be noted that simulated b_{bp}/a_p ratios ranged over one order of magnitude and this might exaggerate its natural variability. Field measurements of $b_{bp}(850)$ performed in RdP varied between 0.45 and 0.93 m^{-1} with a mean value of 0.59 m^{-1} and *SPM* values ranged between 30 and 120 g m^{-3} (Doxaran per. comm.). In turn, measurements of the particulate absorption in the NIR are technically challenging and usually assumed to be negligible (Babin & Stramski, 2004; Stramski, Wozniak, & Flatau, 2004; Stramski, Babin, & Wozniak, 2007). However, a recent study proposed a new technique that allows more precise measurements in the NIR where particulate absorption is low but significant (Röttgers & Gehnke, 2012). Moreover, non-zero particulate absorption in the NIR has been recently measured in river samples and even in algal cultures (Röttgers et al., 2014). They found values reaching as high as pure water absorption in samples from the Elb River in Germany (*e.g.* 1.7 m^{-1} at 850 nm). If we estimate a_p^* (850) using Eq. (3), typical values of a_p^* (443) and *S* found in the literature for coastal waters (Babin, Stramski, et al., 2003), and measured b_{bp}^* (850) values in RdP, the estimated b_{bp}/a_p varied between 20 and 60 with a mean value of ~35. Thus, more precise and simultaneous field measurements of b_{bp} and a_p in the NIR are needed to constrain the expected natural variability, which most probably would reduce the algorithm uncertainty to less than 10%.

The dataset presented in this study includes *in situ* measurements from very different coastal and shallow estuarine environments characterized by high concentrations of suspended sediments and different environmental conditions. Even though it might not be representative of all turbid coastal waters, the algorithm generally performed well for each and all of the sites together. It should be noted, however, that reflectance at 859 nm was more variable for *T* above 500 FNU (Fig. 7) and modeled *T* was thus more scattered around the 1:1 line (Fig. 8a). The sensitivity of one-band algorithms has been shown to depend on both wavelength and turbidity range, with reflectance at shorter wavebands more sensitive to low *T* and longer wavebands to high *T* (Nechad et al., 2010; Ouillon et al., 2008; Shen et al., 2010). This is supported by the results found in the present study showing a general good performance of the proposed algorithm with low mean relative errors (<14%) and *RMSE* (20%) for *T* ranging from 1 to 1000 FNU. This switching band algorithm makes use of the red 645 nm band for low *T* (T ~ 15 FNU or $\rho_w(645) < 0.05$) and the NIR 859 nm band for high *T* values (up to 1000 FNU), while it tends to saturate above 1000 FNU.

4.2. Generality of the 645 nm band algorithm

Even though the analysis of the general validity of the algorithm for low to medium turbidity, *i.e.* using the 645 nm band, was beyond the objectives of the present work, possible sources of error due to variable SIOPs found in regions other that the one used to calibrate the algorithm (SNS) are discussed in the following paragraphs. Error in the *T* retrieval due to variability in CDOM and mass-specific particulate (non-algal and phytoplankton particles) absorption coefficient are analyzed.

Variability in CDOM absorption results in a proportional error in *T* retrieval given its linear dependence in Eq. (1) through A_T coefficient (see Eq. A4 in Appendix A). Similar to the error analysis performed in Nechad et al. (2010), the relative error associated with CDOM absorption was calculated and showed to vary between 0.08 and 18% at

645 nm for typical a_{CDOM} values calculated assuming an exponential dependence with wavelength (Bricaud et al., 1981) for two different exponential slope parameters (0.0176 nm^{-1} and 0.0131 nm^{-1}) and two levels of CDOM absorption (a_{CDOM}(443 nm) = 0.1 m^{-1} and 1.0 m^{-1}).

Previous theoretical analysis indicates that the algorithm's sensitivity to variable mass-specific particulate absorption has negligible impact on derived T in the low reflectance regime of Eq. (1) given that the A_T coefficient does not depend on particulate absorption (Eq. A4), but becomes an additional source of error for high reflectance values (Nechad et al., 2010). The authors found that errors associated with non-algal particulate absorption are generally low for $\lambda > 600$ nm and varied between −1 and −14% at 600 nm for SPM = 10 mg l^{-1} and 100 mg l^{-1}, respectively. Errors associated with the phytoplankton absorption may be significant for high Chl-a > 30 mg m^{-3} at 645 nm, varying between 19% and 57% for Chl-a = 10 mg m^{-3} and 30 mg m^{-3}, respectively following the methodology of Nechad et al. (2010).

5. Conclusions

In the present study we showed that single-band semi-analytical algorithm using 645 nm and 859 nm bands (Dogliotti et al., 2011; Nechad et al., 2009) and a switching scheme can be used to retrieve turbidity from water reflectance in very different regions and is almost insensitive to the sediment type. The impact of the regional variability of the relationship between T and ρ_w(859) caused by natural SPF variability was assessed using radiative transfer simulations. These simulations showed that the corresponding retrieval uncertainty is expected to be low, less than 6%, for very different SPFs typically found in natural coastal waters. The uncertainty on turbidity retrieval associated with bidirectional effects was also analyzed and it was found to be low, typically less than 6%. Considering that technical differences between the instruments used to measure turbidity exists, protocols and specifications of critical components of turbidimeters should be tightened, choosing a set of specifications that are best suited for retrieving the particle side-scattering optical property which has been shown to be less sensitive to varying SPFs and thus useful to retrieve T from remote sensing data. Similarly if the proposed algorithm is used globally, then the turbidity retrieved corresponds strictly to the ISO-based instrument used for algorithm calibration.

A good agreement between modeled and *in situ* measurements was found for each sampled site where T was modeled with *RSME* of 5–33 FNU. A satisfactory performance of the algorithm was also found when all the sites were analyzed together, covering a wide range of T (1.8–988 FNU), and showing a high correlation (r = 0.97), a mean relative error of 13.7%, and bias of 4.8%.

Results presented in this study suggest that a general algorithm can be found for remote sensing of water turbidity using the red and NIR bands of past, present and future ocean color satellite sensors provided atmospheric correction is possible. The use of the 860 nm band on sensors such as MODIS, MERIS, SeaWIFS, GOCI, OLCI, and HICO supposes that a suitable atmospheric correction can be performed there. While this band is generally used precisely for atmospheric correction purposes, it is essential to use an algorithm adapted for turbid waters, giving a non-zero water reflectance either by use of a near infrared marine model (Bailey, Franz, & Werdell, 2010; Doerffer & Schiller, 2007; Moore, Aiken, & Lavender, 1999; Ruddick, Ovidio, & Rijkeboer, 2000; Stumpf, Arone, Gould, & Ransibrahmanakul, 2003), or by use of short wave infrared (SWIR) bands, when available (MODIS) (Wang, Shi, & Tang, 2011; Wang, Tang, & Shi, 2007). The high resolution bands of the MODIS sensor, like the 645 nm and 859 nm bands, that were originally designed for land and cloud applications have the advantage that they do not saturate over highly turbid waters, but have significantly lower sensitivity (low signal-to-noise ratio) relative to the ocean bands (Franz et al., 2006). For example, Petus et al. (2010) showed that MODIS 859 nm band is not sensitive enough to detect turbidity variations between 0.01 and 10 FNU. Thus, in order to overcome this limitation the use of a shorter wavelength, like the 645 nm band, was here proposed to estimate T in medium to low turbid waters.

The main limitation of this algorithm is related to the range of T rather than the geographic region or particle type. On the data set analyzed, the algorithm is suitable for the 1–1000 FNU turbidity range. However, further analysis of the generality of the algorithm for low T, *i.e.* using the 645 nm band, is required in order to evaluate its sensitivity to variable SPF and bidirectional effects.

Finally, suspended particulate matter concentration, the parameter of main interest in sediment transport studies, could subsequently be retrieved by ocean color remote sensing if a region-specific relation between T and *SPM* is known, *i.e.* the global algorithm to retrieve T from reflectance is supplemented with a local algorithm to estimate *SPM* from T. This has the very practical advantage that *SPM* maps could be obtained from different coastal and estuarine waters using relatively inexpensive and portable nephelometers and *SPM* analysis to regionally calibrate just the *T-SPM* relation. This would avoid the need of the more expensive radiometric measurements and restrictive illumination conditions (daylight, cloud-free sky) that are needed to calibrate the full reflectance-*SPM* relationship in any new region. This is similar to the approach suggested by Doerffer (2006) except that the latter study uses total scattering as the retrieved optical parameter whereas our results suggest that uncertainty related to SPF variability is reduced by using b_{90p} instead of b_p.

Acknowledgments

This study was funded by the Belgian Science Policy Office (BELSPO) under the STEREO program SeaSWIR contract (SR/00/156) and the BELCOLOUR-ARG mobility grant. The president and staff of the “Club de Pescadores de Palermo” are thanked for their support, kind help, and good predisposition during field campaigns at the fishermen pier in Buenos Aires, Argentina. We are grateful to three anonymous reviewers for their helpful comments and suggestions.

Appendix A. Turbidity algorithm

The one-band turbidity algorithm used in the present work is briefly described in this appendix, more detailed analysis of the theoretical basis can found in Nechad et al. (2009, 2010) The algorithm relates turbidity (T) to water reflectance (ρ_w) through

$$T = \frac{A_T^{\lambda}\rho_w(\lambda)}{\left(1-\rho_w(\lambda)/C^{\lambda}\right)} \quad [\text{FNU}] \tag{A1}$$

where A_T and C are two wavelength-dependent calibration coefficients. For simplicity, wavelength (λ) will be dropped hereafter. The parameter C is the asymptotic limit of Eq. (1) where T tends to infinity. It is determined only by the type of particles and not by their concentration and is given by

$$C = \gamma\frac{b^*_{bpT}}{a^*_{pT} + b^*_{bpT}} \quad [\text{dimensionless}] \tag{A2}$$

where a^*_{pT} and b^*_{bpT} are the turbidity-specific particulate absorption and backscattering coefficients, and γ is a factor relating reflectance to inherent optical properties

$$\gamma = \pi\Re\frac{f'}{Q} \tag{A3}$$

where $\Re$ represents reflection and refraction effects at the surface (Morel & Gentili, 1996), f' is a varying dimensionless factor (Morel &

Gentili, 1991), and Q is the ratio of subsurface upwelling irradiance to the subsurface upwelling radiance in the viewing direction. Taking typical values of these variables $\gamma = 0.216$ (see Nechad et al., 2009 for details). The A_T factor is the slope of the linear approximation of Eq. (1) for low T and is related theoretically to inherent optical properties by

$$A_T = \frac{a_{np}}{\gamma b^*_{bpT}} \quad [\mathrm{FNU}] \tag{A4}$$

where a_{np} is the non-particulate absorption coefficient, the sum of absorption from pure water and the colored dissolved organic matter absorption coefficient (a_{CDOM}). The parameter C was calibrated using "standard" inherent optical properties (IOPs) since errors in calibration of C have negligible impact in the linear regime of Eq. (1) where the algorithm is used. Thus, average coefficients and typical IOPs for coastal waters found in the literature were used (more details in Nechad et al., 2010). The A_T coefficient was obtained by a non-linear least-square regression analysis using *in situ* measurements of T and ρ_w.

References

Allen, G. P., Salomon, J. C., Bassoullet, P., Du. Penhoat, Y., & Degranpré, C. (1980). Effects of tides on mixing and suspended sediment transport in macrotidal estuaries. *Sedimentary Geology*, *26*, 69–90.

Anderson, C. W. (2006). Turbidity (ver. 2.1): U.S. Geological Survey Techniques of Water-Resources Investigations. book 9, chap. A6., sec. 6.7, July 2006, accessed July 31, 2014, from. http://pubs.water.usgs.gov/twri9A6/

Arndt, S., Vanderborght, J. -P., & Regnier, P. (2007). Diatom growth response to physical forcing in a macrotidal estuary: Coupling hydrodynamics, sediment transport, and biogeochemistry. *Journal of Geophysical Research*, *112*, C05045, http://dx.doi.org/10.1029/2006JC003581.

Babin, M., Morel, A., Fournier-Sicre, V., Fell, F., & Stramski, D. (2003). Light scattering properties of marine particles in coastal and open ocean waters as related to the particle mass concentration. *Limnology and Oceanography*, *48*, 843–859, http://dx.doi.org/10.4319/lo.2003.48.2.0843.

Babin, M., & Stramski, D. (2002). Light absorption by aquatic particles in the near-infrared spectral region. *Limnology and Oceanography*, *47*(3), 911–915.

Babin, M., & Stramski, D. (2004). Variations in the mass-specific absorption coefficient of mineral particles suspended in water. *Limnology and Oceanography*, *49*, 756–767.

Babin, M., Stramski, D., Ferrari, G. M., Claustre, H., Bricaud, A., Obolensky, G., et al. (2003). Variations in the light absorption coefficients of phytoplankton, nonalgal particles and dissolved organic matter in coastal waters around Europe. *Journal of Geophysical Research*, *108*(C7), 3211, http://dx.doi.org/10.1029/2001JC000882.

Bailey, S., Franz, B., & Werdell, J. (2010). Estimation of near-infrared water-leaving reflectance for satellite ocean color data processing. *Optic Express*, *18*(7), 7521–7527.

Barter, P. J., & Deas, T. (2003). Comparison of portable nephelometric turbidimeters on natural waters and effluents. *New Zealand Journal of Marine and Freshwater Research*, *37*, 485–492.

Boss, E., Pegau, W. S., Gardner, W. D., Zaneveld, J. R. V., Barnard, A. H., Twardowski, M. S., et al. (2001). The spectral particulate attenuation and particle size distribution in the bottom boundary layer of a continental shelf. *Journal of Geophysical Research*, *106*, 9509–9516.

Boss, E., Pegau, W. S., Twardowksi, M., Shybanov, E., Korotaev, G., & Baratange, F. (2004). Particulate backscattering ratio at LEO 15 and its use to study particle composition and distribution. *Journal of Geophysical Research*, *109*(C01014).

Bowers, D.G., Boudjelas, S., & Harker, G. E. L. (1998). The distribution of fine suspended sediments in the surface waters of the Irish Sea and its relation to tidal stirring. *International Journal of Remote Sensing*, *19*(14), 2789–2805.

Bricaud, A., Morel, A., & Prieur, L. (1981). Absorption by dissolved organic matter of the sea (yellow substance) in the UV and visible domains. *Limnology and Oceanography*, *26*(1), 43–53.

Bustamante, J., Pacios, F., Diaz-Delgado, R., & Aragonés, D. (2009). Predictive models of turbidity and water depth in the Doñana marshes using LANDSAT TM and ETM + images. *Journal of Environmental Management*, *90*, 2219–2225.

C.A.R.P. (1989). *Estudio para la evaluación de la contaminación en el Río de la Plata. Capítulo I. Aspectos Geológicos.* Buenos Aires: Comisión Administradora del Río de la Plata, 1–72.

Chami, M., McKee, D., Leymarie, E., & Khomenko, G. (2006). Influence of the angular shape of the volume scattering function and multiple scattering on remote sensing reflectance. *Applied Optics*, *45*, 9210–9220.

Chen, Z., Muller-Karger, F., & Hu, C. (2007). Remote sensing of water clarity in Tampa Bay. *Remote Sensing of Environment*, *109*, 249–259, http://dx.doi.org/10.1016/ j.rse.2007.01.002.

Choubey, V. K. (1992). Correlation of turbidity with Indian Remote Sensing Satellite-1A data. *Hydrological Sciences*, *37*(2), 129–140.

Doerffer, R. (2006). How to determine IOPs from MERIS data. *Proceedings of the Second Working Meeting on MERIS and AATSR Calibration and Geophysical Validation (MAVT-2006), 20–24 March 2006, ESRIN, Frascati, Italy (ESA SP-615, July 2006)*.

Doerffer, R., & Schiller, H. (2007). The MERIS case 2 water algorithm. *International Journal of Remote Sensing*, *28*, 517–535.

Dogliotti, A. I., Ruddick, K., Nechad, B., Lasta, C., Mercado, A., Hozbor, C., et al. (2011). Calibration and validation of an algorithm for remote sensing of turbidity over La Plata River estuary, Argentina. *EARSeL eProceedings*, *10*(2), 119–130.

Doxaran, D., Ehn, J., Bélanger, S., Matsuoka, A., Hooker, S., & Babin, M. (2012). Optical characterisation of suspended particles in the Mackenzie River plume (Canadian Arctic Ocean) and implications for ocean colour remote sensing. *Biogeosciences*, *9*, 3213–3229, http://dx.doi.org/10.5194/ bg-9-3213-2012.

EPA, U.S.E.P.A (1993). *Method 180.1 — Determination of turbidity by nephelometry (revision 2.0)*. , 10 (Cincinnati).

European Union (2008). Directive 2008/56/EC of the European Parliament and of the Council of 17 June 2008 establishing a framework for community action in the field of marine environmental policy (Marine Strategy Framework Directive). *Official Journal of the European Union*, *164*, 19–40.

Franz, B.A., Werdell, P. J., Meister, G., Kwiatkowska, E. J., Bailey, S. W., Ahmad, Z., & McClain, C. R. (2006). MODIS land bands for ocean remote sensing applications. *Proc. Ocean Optics XVIII, Montreal, Canada, 9–13 October 2006*.

Froidefond, J. M., Lahet, F., Doxaran, D., Prost, M. T., & Ternon, J. F. (2004). Mudflats and mud suspension observed from satellite data in French Guiana. *Marine Geology*, *208*, 153–168.

Gippel, C. J. (1995). Potential of turbidity monitoring for measuring the transport of suspended solids in streams. *Hydrological Processes*, *9*, 83–97.

Gohin, F. (2011). Annual cycles of chlorophyll-a, non-algal suspended particulate matter, and turbidity observed from space and in-situ in coastal waters. *Ocean Science*, *7*, 705–732.

Gohin, F., Druon, J. N., & Lampert, L. (2002). A five channel chlorophyll algorithm applied to SeaWiFS data processed by SeaDAS in coastal waters. *International Journal of Remote Sensing*, *23*, 1639–1661.

Gohin, F., Loyer, S., Lunven, M., Labry, C., Froidefond, J. -M., Delmas, D., et al. (2005). Satellite-derived parameters for biological modelling in coastal waters: Illustration over the eastern continental shelf of the Bay of Biscay. *Remote Sensing of Environment*, *95*, 29–46.

Goodin, D.G., Harrington, J. A., Jr., Druane Nellis, M., & Rundquist, D. C. (1996). Mapping reservoir turbidity patterns using SPOT-HRV data. *Geocarto International*, *11*(4), 71–78.

Gordon, H. R., Brown, O. B., Evans, R. H., Brown, J. W., Smith, R. C., Baker, K. S., et al. (1988). A semianalytical radiance model of ocean color. *Journal of Geophysical Research*, *93*(D9), 10909–10924.

International Organization for Standardization (ISO) (1999). *Water quality — Determination of turbidity*. ISO, 7027.

Kou, L., Labrie, D., & Chylek, P. (1993). Refractive indices of water and ice in the 0.65–2.5 μm spectral range. *Applied Optics*, *32*, 3531–3540.

Lewis, J., Eads, R., & Klein, R. (2007). Comparisons of turbidity data collected with different instruments. *Report on a Cooperative Agreement between the California Department of Forestry and Fire Protection and USDA Forest Service — Pacific Southwest Research Station (PSW Agreement #06-CO-11272133-041)*.

Liversedge, L. (2007). *Turbidity mapping and prediction in ice marginal lakes at the Bering Glacier System, Alaska.* (M.S. thesis). University of Michigan, School of Natural Resources and Environment (50 pp.).

Loisel, H., Mériaux, X., Berthon, J. F., & Poteau, A. (2007). Investigation of the optical backscattering ratio of marine particles in relation to their biogeochemical composition in the eastern English Channel and southern North Sea. *Limnology and Oceanography*, *52*, 739–752.

Loisel, H., Poteau, A., Artigas, L. F., Lubac, B., Gardel, A., Cafflaud, J., et al. (2009). Analyze of the inherent optical properties of French Guiana coastal waters for remote sensing applications. *Journal of Coastal Research*, *56*, 1532–1536.

Maltese, A., Capodici, F., Ciraolo, G., & La Loggia, G. (2013). Coastal zone water quality: Calibration of a water-turbidity equation for MODIS data. *European Journal of Remote Sensing*, *46*, 333–347, http://dx.doi.org/10.5721/EuJRS20134619.

Martinez-Vicente, V., Land, P. E., Tilstone, G. H., Widdicombe, C., & Fishwick, J. R. (2010). Particulate scattering and backscattering related to water constituents and seasonal changes in the Western English Channel. *Journal of Plankton Research*, *32*, 603–619, http://dx.doi.org/10.1093/plankt/ fbq013.

Matthews, M. W. (2011). A current review of empirical procedures of remote sensing in inland and near-coastal transitional waters. *International Journal of Remote Sensing*, *32*(21), 6855–6899.

McKee, D., Chami, M., Brown, I., Calzado, V. S., Doxaran, D., & Cunningham, A. (2009). Role of measurement uncertainties in observed variability in the spectral backscattering ratio: A case study in mineral-rich coastal waters. *Applied Optics*, *48*(24), 4663–4675.

Mobley, C. D., & Sundman, L. K. (2008). *Hydrolight 5 Ecolight 5 technical documentation.* Bellevue, WA, 98005: Sequoia Scientific, Incorporated, 95.

Mobley, C. D., Sundman, L. K., & Boss, E. (2002). Phase function effects on oceanic light fields. *Applied Optics*, *41*, 1035–1050.

Moore, G. F., Aiken, J., & Lavender, S. J. (1999). The atmospheric correction of water colour and the quantitative retrieval of suspended particulate matter in case II waters: Application to MERIS. *International Journal of Remote Sensing*, *20*, 1713–1733.

Morel, A. (1974). Optical properties of pure water and pure sea water. Chap. 1. In M. Jerlov, & M. Nielsen (Eds.), *Optical aspects of oceanography* (pp. 1–24). New York: Academic Press.

Morel, A., & Gentili, B. (1991). Diffuse reflectance of oceanic waters: Its dependence on Sun angle as influenced by the molecular scattering contribution. *Applied Optics*, *30*(30), 4427–4438.

Morel, A., & Gentili, B. (1996). Diffuse reflectance of oceanic waters. III. Implication of bidirectionality for the remote-sensing problem. *Applied Optics*, *35*(24), 4850–4862.

Nechad, B., Ruddick, K. G., & Neukermans, G. (2009). Calibration and validation of a generic multisensor algorithm for mapping of turbidity in coastal waters. *SPIE European International Symposium on Remote Sensing, Berlin*.

Nechad, B., Ruddick, K. G., & Park, Y. (2010). Calibration and validation of a generic multisensor algorithm for mapping of total suspended matter in turbid waters. *Remote Sensing of the Environment*, *114*, 854–866.

Neukermans, G. (2012). *Optical in situ and geostationary satellite-borne observations of suspended particles in coastal waters*. Ph.D. dissertation. Université du Littoral - Côte d'Opale, Wimereux, France. p. 210. Academic and Scientific Publishers, Ravensteingalerij 28, 1000 Brussels, Belgium. ISBN 978 90 7028 949 2.

Neukermans, G., Loisel, H., Mériaux, X., Astoreca, R., & McKee, D. (2012). *In situ* variability of mass specific beam attenuation and backscattering of marine particles with respect to particle size, density and composition. *Limnology and Oceanography*, *75*(1), 124–144.

Odermatt, D., Gitelson, A., Brando, V. E., & Schaepman, M. (2012). Review of constituent retrieval in optically deep and complex waters from satellite imagery. *Remote Sensing of Environment*, *118*, 116–126.

Ouillon, S., Douillet, P., Petrenko, A., Neveux, J., Dupouy, C., Froidefond, J. -M., et al. (2008). Optical algorithms at satellite wavelengths for total suspended matter in tropical coastal waters. *Sensors*, *8*, 4165–4185.

Petus, C., Chust, G., Gohin, F., Doxaran, D., Froidefond, J. -M., & Sagarminaga, Y. (2010). Estimating turbidity and total suspended matter in the Adour River plume (South Bay of Biscay) using MODIS 250-m imagery. *Continental Shelf Research*, *30*, 379–392.

Potes, M., Costa, M. J., & Salgado, R. (2012). Satellite remote sensing of water turbidity in Alqueva reservoir and implications on lake modelling. *Hydrology and Earth System Sciences Discussions*, *16*, 1623–1633.

Röttgers, R., Brockmann, C., Doerffer, R., Fischer, J., Hollstein, A., Lavender, S., et al. (2012). The STSE — Water Radiance project. *Final Report (ESA Contract: AO 1-5859/08/NL/CT)* (http://www.brockmann-consult.de/beam-wiki/download/attachments/ 17563679/WaterRadiance_finall_report_20120228.pdf).

Röttgers, R., Dupouy, C., Taylor, B. B., Bracher, A., & Woźniak, S. B. (2014). Mass-specific light absorption coefficients of natural aquatic particles in the near-infrared spectral region. *Limnology and Oceanography*, *59*(5), 1449–1460.

Röttgers, R., & Gehnke, S. (2012). Measurement of light absorption by aquatic particles: Improvement of the quantitative filter technique by use of an integrating sphere approach. *Applied Optics*, *51*(9), 1336–1351.

Ruddick, K. G., De Cauwer, V., Park, Y., & Moore, G. (2006). Seaborne measurements of near infrared water-leaving reflectance — The similarity spectrum for turbid waters. *Limnology and Oceanography*, *51*(2), 1167–1179.

Ruddick, K. G., & Lacroix, G. (2006). Hydrodynamics and meteorology of the Belgian Coastal Zone. In V. Rousseau, Ch. Lancelot, & D. Cox (Eds.), *Current status of eutrophication in the Belgian Coastal Zone* (pp. 1–15). Belgium: Universitaires de Bruxelles Press.

Ruddick, K., Ovidio, F., & Rijkeboer, M. (2000). Atmospheric correction of SeaWiFS imagery for turbid coastal and inland waters. *Applied Optics*, *39*, 897–912.

Shen, F., Verhoef, W., Zhou, Y. X., Salama, M. S., & Liu, X. L. (2010). Satellite estimates of wide-range suspended sediment concentrations in Changjiang (Yangtze) estuary using MERIS data. *Estuaries and Coasts*, *33*(6), 1420–1429.

Snyder, W. A., Arnone, R. A., Davis, C. O., Goode, W., Gould, R. W., Ladner, S., et al. (2008). Optical scattering and backscattering by organic and inorganic particulates in U.S. coastal waters. *Applied Optics*, *47*(5), 666–677.

Stramski, D., Babin, M., & Wozniak, S. (2007). Variations in the optical properties of terrigeneous mineral-rich particulate matter suspended in seawater. *Limnology and Oceanography*, *52*, 2418–2433.

Stramski, D., Wozniak, S. B., & Flatau, P. J. (2004). Optical properties of Asian mineral dust suspended in seawater. *Limnology and Oceanography*, *49*, 749–755.

Stumpf, R. P., Arone, R. A., Gould, R. W., & Ransibrahmanakul, V. (2003). A partially coupled ocean-atmosphere model for retrieval of water-leaving radiance from SeaWiFS in coastal waters. In S. B. Hooker, & E. R. Firestone (Eds.), *SeaWiFS Postlaunch Technical Report Series*, *Vol. 22*. (pp. 51–59). Greenbelt, Maryland: NASA Goddard Space Flight Center (Chap.9, NASA/TM-2003-206892).

Sullivan, J. M., & Twardowski, M. S. (2009). Angular shape of the volume scattering function in the backward direction. *Applied Optics*, *48*, 6811–6819.

Tzortziou, M., Herman, J., Gallegos, C., Neale, P., Subramaniam, A., Harding, L., et al. (2006). Bio-optics of the Chesapeake Bay from measurements and radiative transfer closure. *Estuarine, Coastal and Shelf Science*, *68*(2), 348–362.

Urien, C. M. (1967). *Los sedimentos modernos del Río de la Plata Exterior. Servicio de Hidrografía Naval, Argentina, Público H-106*, *4*. (pp. 113–213), 113–213.

Wang, M., Shi, W., & Tang, J. (2011). Water property monitoring and assessment for China's inland Lake Taihu from MODIS-Aqua measurements. *Remote Sensing of Environment*, *115*, 841–854.

Wang, M., Tang, J., & Shi, W. (2007). MODIS-derived ocean color products along the China east coastal region. *Geophysical Research Letters*, *34*, L06611.

Whitmire, A. L., Boss, E., Cowles, T. J., & Pegau, W. S. (2007). Spectral variability of the particulate backscattering ratio. *Optics Express*, *15*(11), 7019–7031.